Gorerite, $CaAlFe_{11}O_{19}$, a new mineral of the magnetoplumbite group from the Negev Desert, Israel

Evgeny V. Galuskin[1]*, Biljana Krüger[2], Irina O. Galuskina[1], Hannes Krüger[2], Krzysztof Nejbert[3] and Yevgeny Vapnik[4]

[1]Institute of Earth Sciences, Faculty of Natural Sciences, University of Silesia, Będzińska 60, 41-200 Sosnowiec, Poland

[2]Institute of Mineralogy and Petrography, University of Innsbruck, Innrain 52, 6020 Innsbruck, Austria

[3]Faculty of Geology, University of Warsaw, Żwirki i Wigury 93, 02–089 Warszawa, Poland

[4]Department of Geological and Environmental Sciences, Ben-Gurion University of the Negev, POB 653, Beer-Sheva 84105, Israel

* Correspondence: evgeny.galuskin@us.edu.pl

Abstract

Gorerite, ideally $CaAlFe_{11}O_{19}$ is a new mineral and M-type hexaferrite of the magnetoplumbite group. It was found in ferrite-rich segregations of esseneite-gehlenite-wollastonite-anorthite melted rock of the 'olive' subunit of pyrometamorphic rocks located near Hatrurim Junction in the Negev Desert, Israel. Within these ferrite-rich segregations up tu 100 μm in size, platy

This is a 'preproof' accepted article for Mineralogical Magazine. This version may be subject to change during the production process.
DOI: 10.1180/mgm.2024.30

crystals of gorerite up to 50 μm in size intergrow with hibonite, hematite, maghemite, magnesioferrite, dorrite, barioferrite, and andradite, forming aggregates. Additionally, small crystals of gorerite occur within magnesioferrite. Importantly, gorerite did not directly crystallize from the melt. Instead, it emerged through a reaction involving earlier crystallized hibonite and an iron-enriched melt, resulting in the partial or complete replacement of hibonite by gorerite. Gorerite appears grey in the reflected light (R = 18-23%), displaying distinct bireflectance: dark-grey perpendicular to *Z*, light-grey parallel to *Z*. Its Raman spectrum exhibits only one strong band at 700 cm^{-1}, which shifts to higher frequencies with increasing Al content. Gorerite crystallizes in the $P6_3/mmc$ space group, with lattice parameters a = 5.8532(4)Å, c = 22.7730(2)Å, and V = 675.67(7) $Å^3$ with Z = 2. It exhibits a structure characterized by an intercalation of triple spinel-like S-blocks and rock-salt type R-blocks along the hexagonal c-axis.

Keywords: gorerite; new mineral; structure; Raman; magnetoplumbite group; Hatrurim, Israel

Introduction

The newly discovered mineral gorerite, with the ideal chemical formula $CaAlFe_{11}O_{19}$, represents an addition to the magnetoplumbite group. This group encompasses minerals characterized by the general formula $AB_{12}O_{19}$, where the cations ***A*** may include elements such as Ba, Pb, Ca, or K, while the ***B*** cations can include Mg, Al, Ti, Cr, Mn, Fe, Zn, Sb, among others (Pullar, 2012; Holtstam and Hålenius, 2020). Recent classification schemes have further refined this group by categorizing it based on the predominant composition at the ***A***-site (Holtstam and Hålenius, 2020). With calcium occupying the ***A***-site, gorerite, along with hibonite ($CaAl_{12}O_{19}$), constitutes the hibonite subgroup within the magnetoplumbite group.

https://doi.org/10.1180/mgm.2024.30 Published online by Cambridge University Press

The minerals belonging to the magnetoplumbite group exhibit structures characterized by an intercalation of two types of blocks along the hexagonal c-axis: **S** (spinel-like) blocks and **R** (rock salt type) blocks. The S-blocks demonstrate a *ccp* (closest-packed cubic) arrangement of atoms with an overall composition of $\{B_9O_{12}\}^{3+}$. On the other hand, the R-blocks possess an *hcp* (hexagonal close-packed) structure with an overall composition of $\{AB_3O_7\}^{3-}$. The stacking sequence is denoted as ·RSR*S*·, where the asterisk symbol indicates that certain blocks are rotated by 180° to maintain $P6_3/mmc$ symmetry.

Gorerite was initially described as 'hexaferrite' and was first discovered in flamite-gehlenite hornfels located at the Jabel Harmun locality in the West Bank (Galuskina et al., 2017). However, due to the limited size of the grains, structural analysis could not be conducted on this particular sample. The holotype gorerite discussed here was found in esseneite-gehlenite-wollastonite-anorthite melted rock within the 'olive' subunit of pyrometamorphic rocks, as illustrated in Figure 1C of Kruszewski et al. (2021). These 'olive' subunits are currently known to exist solely within the northern region of the Hatrurim Basin, located in the Negev Desert, Israel (Gross, 1977).

It's worth noting that outcrops of Jabel Harmun in the West Bank, as well as those of the Hatrurim Basin in the Negev Desert, are part of a larger geological unit known as the Hatrurim Complex. The Hatrurim Complex, also referred to as the 'Mottled Zone' or 'Hatrurim Formation', comprises numerous other outcrops scattered across the South Levant territory on both sides of the Dead Sea Rift (Bentor, 1960; Gross, 1977; Novikov et al., 2013; Galuskina et al., 2014).

Aside from gorerite, the Hatrurim Basin serves as the type locality for barioferrite ($BaFe_{12}O_{19}$), another mineral belonging to the magnetoplumbite group. Barioferrite was initially identified in altered baryte concretions (Murashko et al., 2011). Both gorerite and barioferrite are

https://doi.org/10.1180/mgm.2024.30 Published online by Cambridge University Press

relatively widespread in rocks found within the Hatrurim Basin. These minerals typically occur as small plate inclusions within magnesioferrite from gehlenite-larnite (flamite) hornfels and rankinite-schorlomite paralava (Galuskina et al., 2017).

In addition to barioferrite and gorerite, hibonite ($CaAl_{12}O_{19}$) has been discovered in hematite segregations from the paralava of the 'olive' unit (Sharygin, 2019). Minerals of the magnetoplumbite group within the Hatrurim Complex exhibit notable variations in magnesium, titanium, and chromium contents (Sharygin, 2019; Sharygin and Murashko, 2021; Krüger et al., 2021). Furthermore, recently discovered β-alumina-type minerals, namely kahlenbergite ($KAl_{11}O_{17}$) and shagamite ($KFe^{3+}_{11}O_{17}$), have been found in association with hibonite and gorerite (Krüger et al., 2021; Galuskin et al., 2021). Additionally, it's worth noting that although the β-alumina-type minerals were previously classified within the magnetoplumbite group, they are not currently included in the present nomenclature due to the requirement of isostructurality (Holtstam and Hålenius, 2020).

Within the R-type blocks of the magnetoplumbite structure, one of the smaller B-cations is five-coordinated. However, in the structure of β-alumina-type minerals, the smaller cations are tetrahedrally coordinated (Krüger et al., 2021). This difference in coordination geometry contributes to the exclusion of β-alumina-type minerals from the current classification, as they do not exhibit the same structural topology as magnetoplumbite minerals.

The mineral gorerite (abbreviated Gor), has been officially approved by the Commission on New Minerals, Nomenclature and Classification (CNMNC) of the International Mineralogical Association (IMA) under the number IMA 2019-080. Gorerite is named after Wadi Gorer in the Negev Desert, Israel. This wadi is situated in close proximity to the Hatrurim Junction along the road connecting Arad City with the Dead Sea, near the type locality of gorerite.

https://doi.org/10.1180/mgm.2024.30 Published online by Cambridge University Press

The type material, which comprises a portion of the holotype specimen, has been deposited in the mineralogical collection of the Fersman Mineralogical Museum, located at Leninskiy pr., 18/k2, 115162 Moscow, Russia. It is cataloged under the number 5420/1.

Methods of investigation

The semi-quantitative composition and morphology of gorerite and associated phases were investigated using scanning electron microscopes Philips XL30 and Phenom XL at the Institute of Earth Sciences, University of Silesia, Poland. Additionally, the chemical composition of minerals was analyzed using the Electron Microprobe Analyzer CAMECA SX100 at the University of Warsaw, Poland, operating in the WDS mode. The analysis parameters were set with an acceleration voltage of 15kV, a beam current of 15 nA, and a beam diameter of approximately 1 μm.

For the analysis of specific elements, the following standards were utilized, with the corresponding *K*α lines in parentheses: albite (Na), orthoclase (K, Na), dolomite (Mg), wollastonite (Ca, Si), rhodonite (Mn), rutile (Ti), V metal (V), celestine (Sr), Cr_2O_3 (Cr), hematite (Fe), and baryte (BaLα).

Raman spectra of gorerite and associated barioferrite and hibonite were collected using a WITec alpha 300R Confocal Raman Microscope at the Institute of Earth Science, University of Silesia, Poland. This microscope is equipped with an air-cooled solid laser operating at 532 nm and a CCD camera set to a temperature of -61°C. Laser radiation was transmitted to the microscope via a single-mode optical fiber with a diameter of 3.5 μm. An air Zeiss LD EC Epiplan-Neofluan DIC-100/0.75NA objective lens was utilized for focusing.

Raman scattered light was directed through a broad-band single-mode fiber with an effective pinhole size of approximately 30 μm and a monochromator featuring a 600 mm^{-1} grating. The

https://doi.org/10.1180/mgm.2024.30 Published online by Cambridge University Press

laser power at the sample position was approximately 10-15 mW. Integration times of 5 seconds with accumulation of 20 scans were selected, resulting in a resolution of 3 cm^{-1}. The monochromator was calibrated using the Raman scattering line of a silicon plate at 520.7 cm^{-1}. These parameters ensured accurate and reliable recording of the Raman spectra for analysis.

Single-crystal diffraction measurements were conducted under ambient conditions utilizing synchrotron radiation with a wavelength of $\lambda = 0.70849$Å. These experiments were carried out at the X06DA beamline located at the Swiss Light Source, Paul Scherrer Institute, Villigen, Switzerland. The data acquisition process was facilitated by the use of the DA+ software, as outlined by Wojdyla et al. (2018). Following data acquisition, determination of lattice parameters was performed using CrysAlisPro (Rigaku, 2022). Subsequently, structure refinement was carried out utilizing Jana2006 software, as described by Petříček et al. (2014).

Occurrence and gorerite description

Samples containing gorerite were collected in 2013 from the 'olive' unit outcrop of the Hatrurim Complex, situated near the Hatrurim junction on the Arad-Dead Sea road in the Negev Desert, Israel (coordinates: N31°13′58″ E35°16′2″), as depicted in Figure 1a. The 'olive' units are characterized by gray-green to yellow-brown to pale yellow rocks consisting of paralava and hornfels. These rocks exhibit distinctive lens-like ferrite rich segregations, as illustrated in Figure 1b (Vapnik et al., 2007; Sharygin, 2019; Galuskin et al., 2019; Krüger et al., 2021).

https://doi.org/10.1180/mgm.2024.30 Published online by Cambridge University Press

Fig.1. (a) Illustration of the distinct 'desert patina' observed on the surface of the 'olive' unit rock, captured at the Hatrurim Junction, Israel. (b) A dark-green rock belonging to the 'olive' unit displays a transition in color to light-brown around the edges of large rock blocks and adjacent to ferrite-rich segregations (as indicated by the arrow). This alteration in coloration is notable and characteristic of rocks within the 'olive' unit.

In the studied samples, three distinct zones are discernible:

1. The ferrite-celsian zone (zone II), characterized by abundant zonal aggregates of ferrites containing gorerite (see Fig. 2). This zone serves as an intermediate area situated between hematite segregations (zone I) and the host rocks (zone III) (see Fig. 2).
2. The hematite zone (zone I), which primarily consists of hematite along with other minerals such as magnesioferrite, maghemite, hibonite, dorrite-khesinite, and barioferrite.
3. The host rocks zone (zone III), comprising pyroxene of the diopside-esseneite series, wollastonite, anorthite, gehlenite, andradite, hematite, and celsian.

Additionally, in the later stages of mineralization, zeolites, ettringite, calcite, and baryte are observed within the studied samples.

https://doi.org/10.1180/mgm.2024.30 Published online by Cambridge University Press

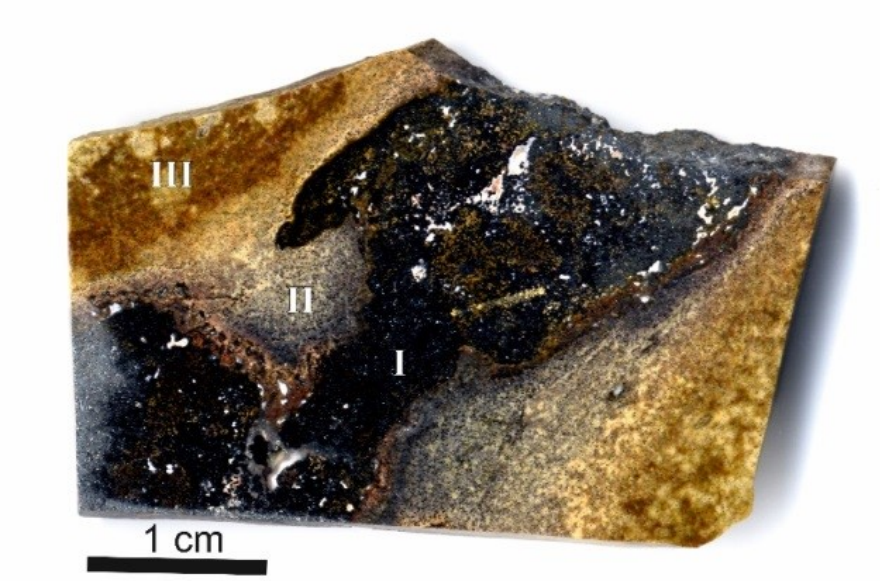

Fig. 2. The holotype specimen depicts a fragment of 'olive' unit paralava enriched in ferrites. The specimen is divided into three distinct zones: I – hematite zone; II – ferrite-celsian zone; III – esseneite-wollastonite zone. These zones represent different mineralogical compositions and serve to delineate the spatial distribution of minerals within the paralava sample.

In the hematite zone (zone I), gorerite was observed as rare, fine plates, typically only a few microns thick. These plates were found to occur within magnesioferrite. In contrast, in zone II, which is characterized by fine symplectites composed of wollastonite, gehlenite, andradite, and esseneite, and enriched with celsian, gorerite is a constituent of the ferrite aggregates. These ferrite aggregates reach sizes of up to 100 μm (Figs. 3, 4, S1).

Ferrite aggregates (Figs. 3b; 4b,c; S1b; 5) can be described as follows: The central part is filled by hematite (sometimes maghemite) which is overgrown by magnesioferrite. Tabular gorerite crystals with hibonite relics are located inside this ferrite aggregate. Fine epitaxial barioferrite zones grow on gorerite. The ferrite aggregates exhibit a fine dorrite rim, which is in turn overgrown by andradite. Small cavities are often located in the central part of the ferrite aggregates and are filled by low-temperature minerals: zeolites, tacharanite, or calcite (Figs. 4, 5).

https://doi.org/10.1180/mgm.2024.30 Published online by Cambridge University Press

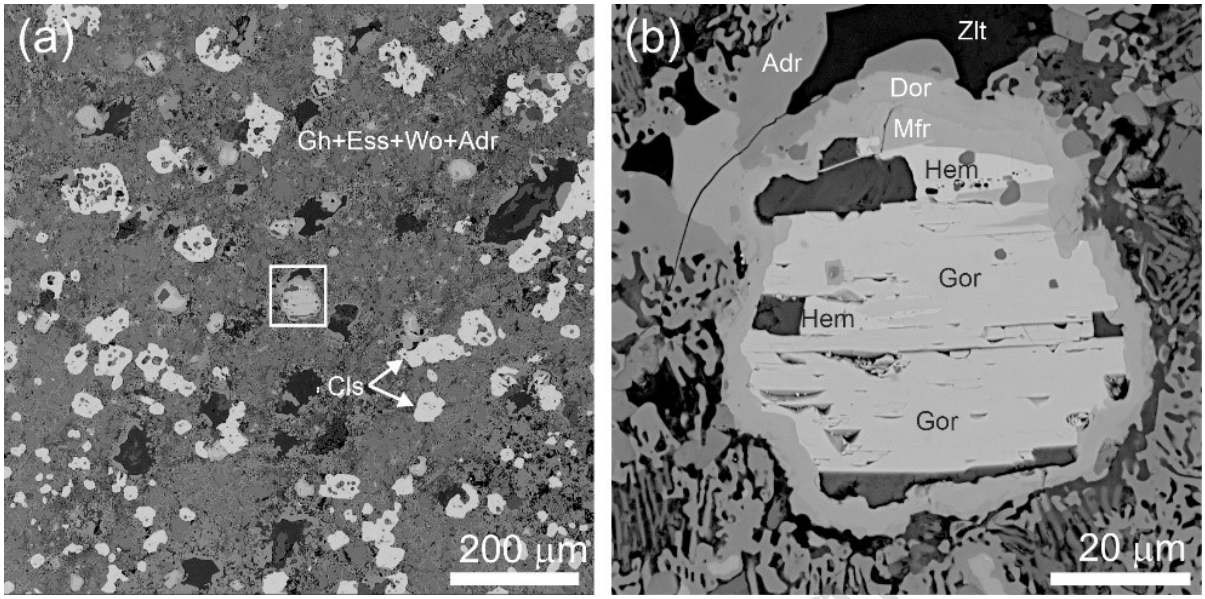

Fig. 3. BSE images of (a) Zone II, as illustrated in Figure 2, characterized by fine symplectites composed of esseneite, wollastonite, gehlenite with relatively big celsian metacrysts and inhomogeneous ferrite aggregates; (b) Depiction of the largest gorerite grains found in the sample. Fragments of these grains were utilized for structural investigation and Raman spectroscopic studies. Adr = andradite, Cls = celsian, Dor = dorrite, Ess = esseneite, Gh = gehlenite-akermanite series, Gor = gorerite, Hem = hematite, Mfr = magnesioferrite, Wo = wollastonite, Zlt = zeolite.

https://doi.org/10.1180/mgm.2024.30 Published online by Cambridge University Press

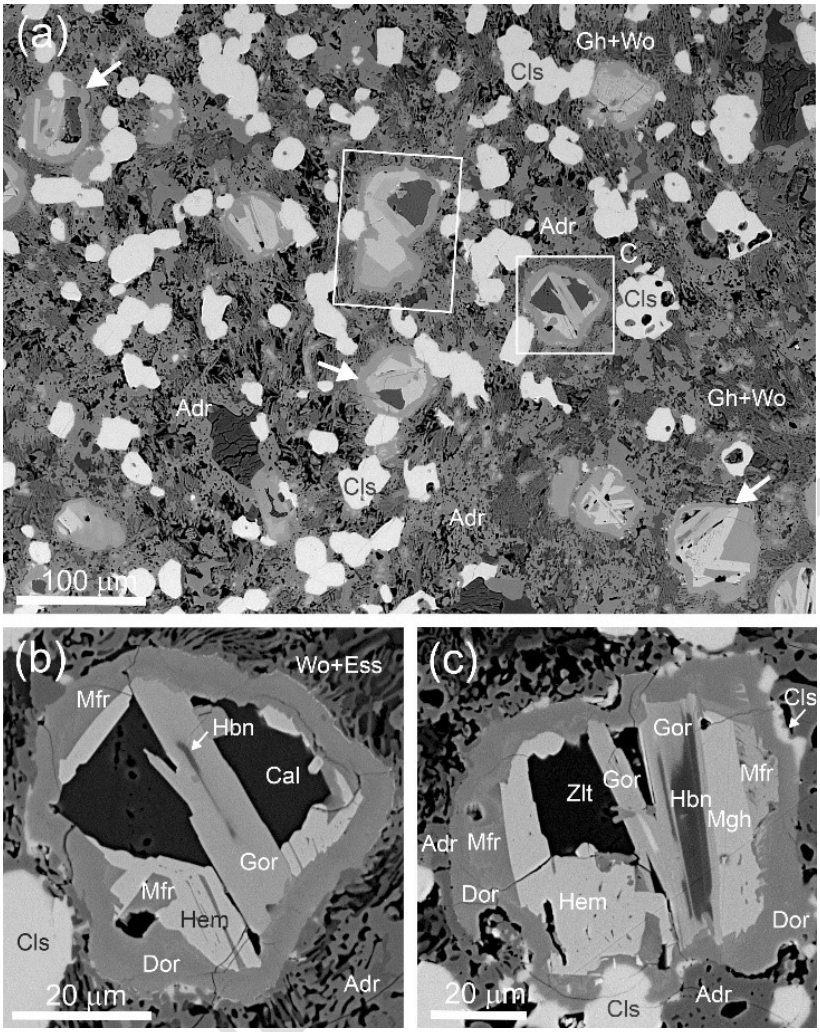

Fig. 4. BSE images of: (a) a relatively high concentration of ferrite aggregates containing gorerite (indicated by white arrows) in zone II, near the contact with the hematite zone (zone I, as shown in Figure 2). A magnified view of a ferrite aggregate is presented in Fig. 4b (enclosed in a white frame). The ferrite aggregate highlighted in a black frame was utilized for optical measurements (see Fig. 5a, b). (b) Gorerite crystals with hibonite relics, as commonly observed. The central part of the aggregate is filled with calcite; (c) Ferrite aggregate containing hematite and maghemite. The general zoning of ferrite aggregates from rim to core includes andradite, dorrite, magnesioferrite, hematite/maghemite, gorerite, and hibonite. Key: Adr = andradite, Cal = calcite, Cls = celsian, Dor = dorrite, Ess = esseneite, Gh = gehlenite-ackermanite series, Gor = gorerite, Hem = hematite, Hbn = hibonite, Mfr = magnesioferrite, Mgh = maghemite, Wo = wollastonite, Zlt = zeolite.

https://doi.org/10.1180/mgm.2024.30 Published online by Cambridge University Press

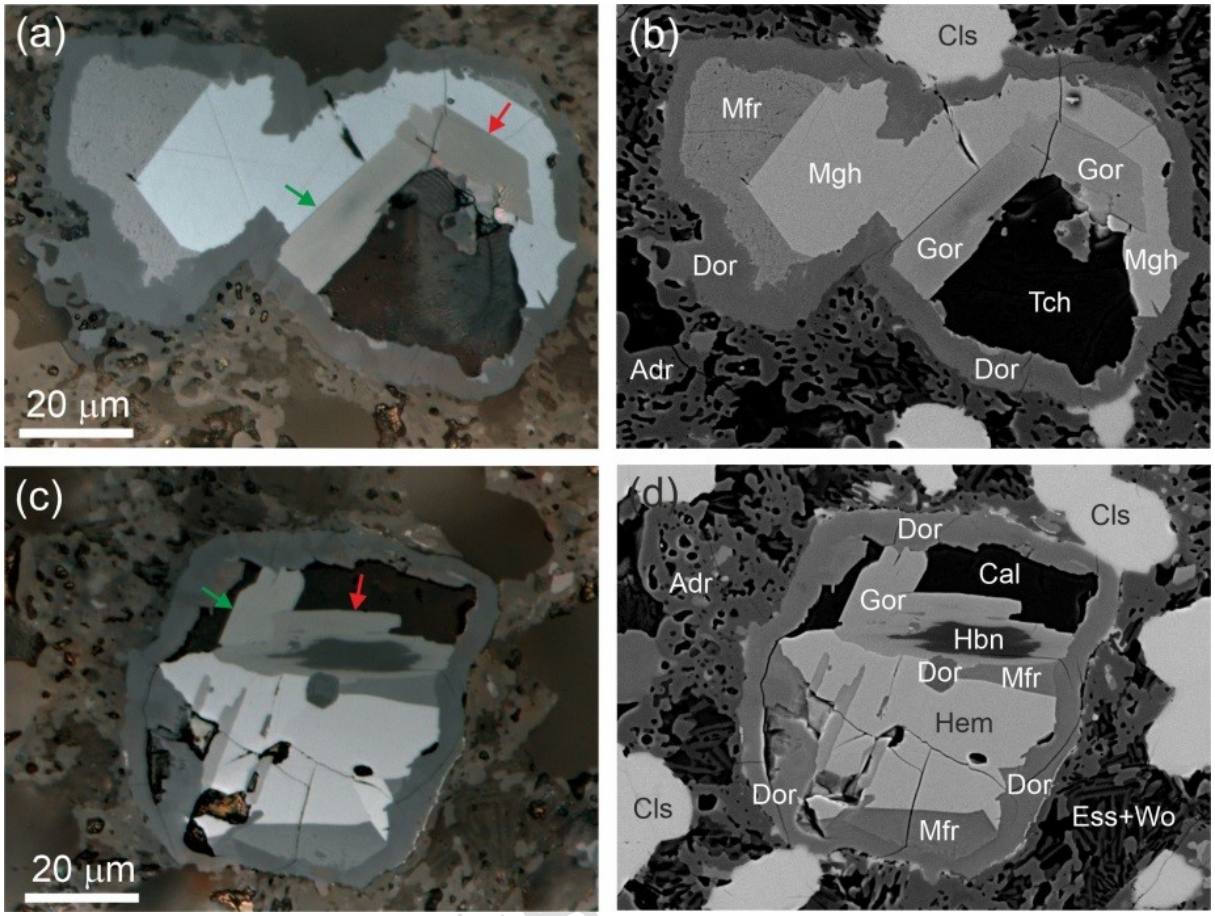

Fig. 5. (a,c) – Gorerite exhibits well-marked bireflectance, which is clearly visible on crystals with different orientations (indicated by green and red arrows). These images were captured under reflected light using plane-polarized light (PPL). (b,d) Backscattered electron (BSE) images of the aggregates shown in Figures 5a and 5c, respectively. The key includes the following abbreviations: Adr = andradite, Cal = calcite, Cls = celsian, Dor = dorrite, Ess = esseneite, Gor = gorerite, Hem = hematite, Hbn = hibonite, Mfr = magnesioferrite, Mgh = maghemite, Tch = tacharanite, Wo = wollastonite.

The gorerite grain selected for single-crystal structural investigation exhibited chemical homogeneity and was characterized by the following empirical formula $(Ca_{0.99}Na_{0.01})_{\Sigma 1.00}(Fe^{3+}_{9.51}Al_{1.46}Ti^{4+}_{0.35}Cr^{3+}_{0.31}Mg_{0.28}Mn^{3+}_{0.05}Ca_{0.04})_{\Sigma 12}O_{19}$ (Table 1, analysis 1; Fig. 3b). Gorerite crystals containing hibonite relics displayed increased Al content and decreased Ti, Cr, and Mg contents. The empirical formulas for these crystals were determined as follows: $Ca_{1.00}(Fe^{3+}_{8.95}Al_{2.49}Ti^{4+}_{0.22}Cr^{3+}_{0.07}Mg_{0.20}Mn^{3+}_{0.02}Ca_{0.04}Si_{0.01})_{\Sigma 12}O_{19}$ (for the crystals in Fig. 4b,c Table 1, analysis 2) and

https://doi.org/10.1180/mgm.2024.30 Published online by Cambridge University Press

$(Ca_{0.99}Ba_{0.01}Sr_{0.01})_{\Sigma 1.01}(Fe^{3+}_{9.00}Al_{2.50}Ti^{4+}_{0.20}Cr^{3+}_{0.05}Mg_{0.18}Mn^{3+}_{0.02}\,Ca_{0.03}Si_{0.01})_{\Sigma 12}O_{19}$ (for the crystals Fig. 5c,d; Table 1, analysis 3).

Hibonite, preserved as relics in gorerite from zone II (Figs. 4c; 6c,d; Table S1, analysis 1), and hibonite intergrown with an unusual high-strontium gorerite-like mineral at the boundary of zones I and II (Fig. S2; Table S1, analysis 2), exhibited higher impurity levels of Mg and Ti compared to gorerite. The high-strontium gorerite-like mineral (Fig. S2b; Table S1, analysis 3) requires further investigations because it is most likely a hexaferrite (of the M-type) with a mixed-type structure (Iyi and Göbbels,1996).

Barioferrite crystallized as the last of the minerals of the magnetoplumbite group, is the most ferrous and its empirical crystal chemical formulas are close to the end-member one (Fig. S2a; Table S1, analyses 4, 5).

Minerals of the oxyspinel group (spinel subgroup) are represented by magnesioferrite and maghemite (Table S2). Maghemite can be readily distinguished from hematite by its light-blue coloration in reflected light (see Fig. 5a) and typically exhibits higher aluminum content (refer to Tables S2, S3).

Gorerite is characterized by its black color with a black streak, occasionally displaying a brown tint and submetallic luster. It forms platy hexagonal crystals with {001} and {100} simple forms, and twins are not observed. The average micro-indentation hardness, based on 18 spot measurements (VHN10), is 718(15), ranging from 692 to 752 kg/mm2, corresponding to a Mohs hardness of 5-6. The cleavage is good on (001), while parting is observed on (100). The tenacity of gorerite is brittle, and its fracture is uneven perpendicular to (001). Density measurements were not conducted due to the small size and rarity of gorerite crystals; however, a density of 5.36 $g \cdot cm^{-3}$ was calculated based on the empirical formula and unit cell volume refined from

https://doi.org/10.1180/mgm.2024.30 Published online by Cambridge University Press

single-crystal XRD data for the holotype specimen. In reflected light, gorerite appears grey, with reflectance values ranging between 18% and 24% (refer to Table S4). The mineral is anisotropic and exhibits well-defined bireflectance: appearing dark-grey perpendicular to Z and light-grey parallel to Z. Additionally, rare brown-red internal reflections may be observed.

Raman spectroscopy

The Raman spectrum of the holotype gorerite reveals the following bands (see Fig. 6; cm^{-1}): 1411, 733, 700, 658, 543, 416, 350, 297, 258, 213, 186, 170 and 89. The most prominent bands correspond to the vibrations of Fe^{3+}-O bonds: 733 cm^{-1} ($\nu_3(FeO_5)$ + $\nu_1(FeO_4)$, 700 cm^{-1} $\nu_1(FeO_5)$, 658 cm^{-1} $\nu_1(FeO_6)$, 543 cm^{-1} $\nu_4(FeO_5)$, 416 ν_4 (FeO_5), 350 cm^{-1} $\nu_2(FeO_5)$ (Kreisel *et al*., 1998; Galuskin *et al*., 2018; Krzątała *et al*., 2018). The band at 186 cm^{-1} is attributed to the vibrations of Ca-O bonds, while the band at 1411 cm^{-1} is an overtone.

In the spectra of minerals belonging to the magnetoplumbite group found in 'olive' unite rocks, the most intense band is associated with vibrations in the trigonal bipyramid within the R-layer and typically falls within the range of 850-600 cm^{-1} (Fig. 6). Specifically, in hibonite $CaAl_{12}O_{19}$, with AlO_5 in R-layers, this band occurs at 841 cm^{-1}, while in barioferrite $BaFe^{3+}{}_{12}O_{19}$, with AlO_5 with minor Al impurity in the in R-layers, the band shifts to 688 cm^{-1} (see Fig. 6). Interestingly, in the high-strontium gorerite-like mineral, this band is split into two distinct bands at 731 and 716 cm^{-1} (see Fig. 6). In the Raman spectrum of the holotype gorerite this band is at 700 cm^{-1}, whereas in Al-bearing gorerite it shifts to 719 cm^{-1}. Undoubtedly, a type of ***A***-cation has influence on the position of this band, too.

https://doi.org/10.1180/mgm.2024.30 Published online by Cambridge University Press

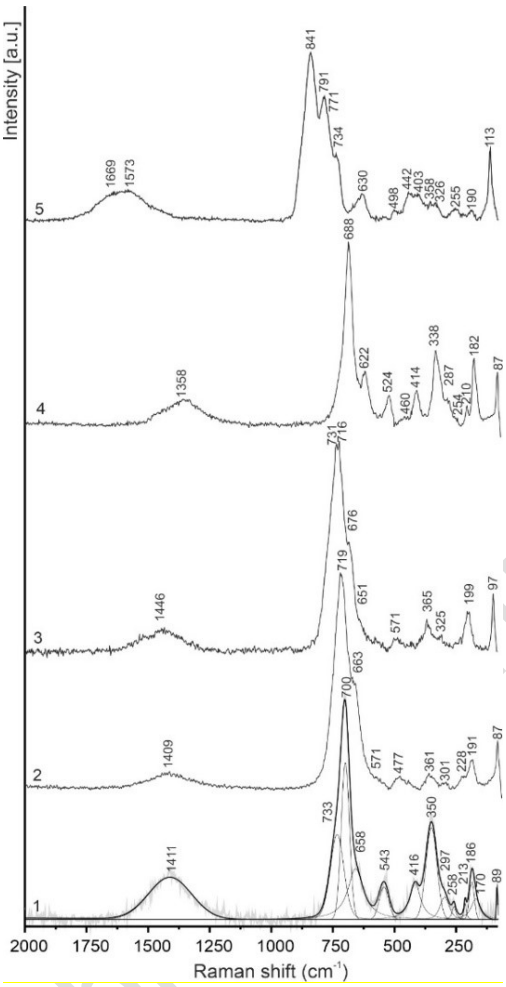

Fig.6. Raman spectra of hexaferrites from „olive" unit rock: 1 - holotype gorerite (Fig. 3b); 2 – gorerite (Fig. 4c); 3 – "Sr-Ba-gorerite" (Fig. S2b); 4 – barioferrite (Fig. S2a); 5 – hibonite (Fig. 5c,d).

Crystal structure

Single-crystal X-ray diffraction data were collected utilizing a very small gorerite crystal fragment measuring 12×10×5 μm in size, employing synchrotron radiation.

The crystal structure refinement process commenced with the atomic coordinates of $CaAl_{12}O_{19}$ (ICSD 202616). The ***A***-site was found to be fully occupied by Ca. Total scattering densities on the remaining five *M*-cation positions (named *M*1to *M*5 in the order given by Holtstam and Hålenius, 2020) were determined through refinement of the individual site occupancies. Specifically, at the five-coordinated site, refinement was conducted for Ti versus Fe, while at the

https://doi.org/10.1180/mgm.2024.30 Published online by Cambridge University Press

other four sites, refinement was performed for Al versus Fe. For comprehensive information regarding the data collection and structure refinement, please refer to Table 2. Final atomic coordinates are provided in Table 3, while anisotropic displacement parameters can be found in Table 4. Additionally, selected bond distances are outlined in Table 5.

The crystal structure of gorerite comprises two fundamental modules, as illustrated in Fig. 7: spinel-like S-blocks and R-blocks. The S-modules are comprised of two identical sheets of edge-shared $M5O_6$ octahedra with an additional octahedral ($M1O_6$)/tetrahedral ($M3O_4$) layer sandwiched between two octahedral layers. Within the S-modules, there are three independent sites: *M*1, *M*3, and *M*5. At the *M*1 site, aluminum predominantly occupies over iron, whereas the *M*3 and *M*5 sites are mainly occupied by Fe^{3+} (Table 3).

Within each R-module, layers are constructed from face-sharing (Fe_2O_9) octahedra (*M*4 site) which are connected by their apical vertices with (FeO_5) trigonal bipyramids at *M*2 site. These layers feature cavities filled by Ca (Ca1) cations (Fig. 7). Notably, unlike structures such as barioferrite, hibonite and others with similar characteristics (Nagashima *et al*., 2010; Krzątała *et al*., 2018), a splitting of the *M*2 site is not observed in gorerite.

Due to the limited amount of pure gorerite, meaningful powder diffraction data could not be collected. Therefore, powder diffraction data were calculated from the structural data obtained through single-crystal analysis Table S5.

https://doi.org/10.1180/mgm.2024.30 Published online by Cambridge University Press

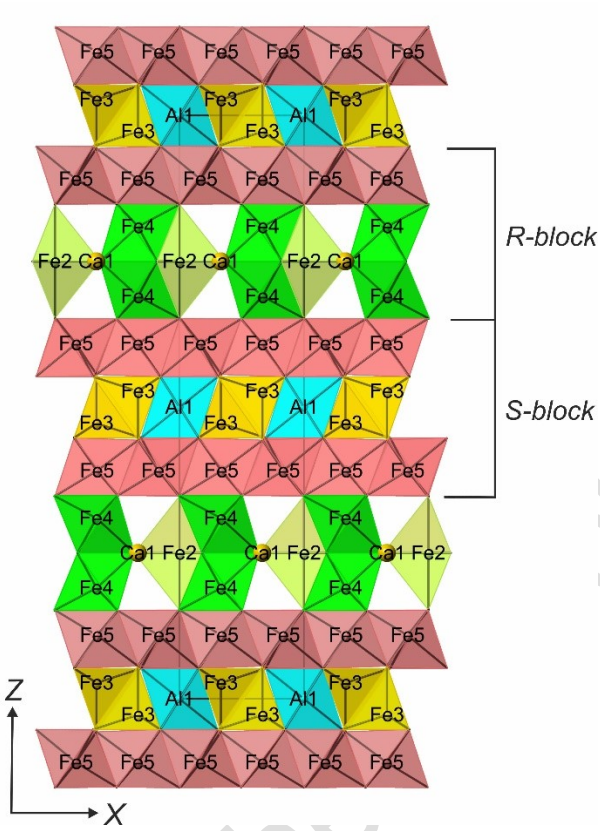

Fig. 7. Gorerite displays a magnetoplumbite-type structure, where spinel-like S-blocks are interspersed with rock salt type R-blocks in the sequence of SRS*R*. The asterisk symbol denotes blocks that are rotated by 180° to maintain a $P6_3/mmc$ symmetry.

Discussion

Structural and nomenclature aspects

The boundary of the R and S blocks, adopted for magnetoplumbite group minerals in this work, passes through the oxygens (polyhedra boundary; Fig. 7), which does not correspond to the generally accepted dividing boundary of these blocks, which passes through the cations at the *M*5 site (Pullar, 2012). Such distinguishing of blocks is due to the fact that the structural models based on oxygen packing are used for hexaferrites (Pullar, 2012). This approach allows for the representation of the magnetoplumbite-type structure as the intercalation of two blocks: $^{R}\{AM_6O_{11}\}^{2-}$ and $^{S}\{M_6O_8\}^{2+}$ (Holtstam and Hålenius, 2020). With respect to the structural sites of magnetoplumbite the block formulas are written as $^{R}\{AM2M4_2M5_3O_{11}\}^{2-}$ and

https://doi.org/10.1180/mgm.2024.30 Published online by Cambridge University Press

$^{S}\{M1M3_2M5_3O_8\}^{2+}$, i.e. the *M*5 site is divided between the two blocks. This complicates the elaboration of the classification scheme of magnetoplumbite group, because the *M*5 positions may contain different cations. In Fig. 7 the polyhedral structural model of gorerite with the boundary of the structural blocks along the polyhedra boundary is shown. In this case, the magnetoplumbite structure can be presented as the intercalation of two blocks: $^{R}\{AM_3O_7\}^{3-}$ and $^{S}\{M_9O_{12}\}^{3+}$, or with respect to the sites – $^{R}\{AM2M4_2O_7\}^{3-}$ and $^{S}\{M1M3_2M5_6O_{12}\}^{3+}$. The structural formula of gorerite can be expressed as follows $^{R}[^{A}Ca^{M2}(Fe_{0.67}Ti_{0.33})^{M4}(Fe_{0.852}Al_{0.148})_2]$ $^{S}[^{M1}(Al_{0.597}Fe_{0.403})^{M3}(Fe_{0.774}Al_{0.226})_2{}^{M5}(Fe_{0.751}Al_{0.249})_6]O_{19}$ = $Ca(Fe_{8.83}Al_{2.84}Ti_{0.33})_{\Sigma 12}O_{19}$. To separate the R and S-Blocks, their respective content is given in square parentheses with left-superscripted R or S.This formulation approximates the empirical formula: $(Ca_{0.99}Na_{0.01})_{\Sigma 1.00}(Fe^{3+}{}_{9.51}Al_{1.46}Ti^{4+}{}_{0.35}Cr^{3+}{}_{0.31}Mg_{0.28}Mn^{3+}{}_{0.05}Ca_{0.04})_{\Sigma 12}O_{19}$. It is notable that the empirical formula contains a lower Al(+Mg) content. Given that all measurements were conducted on a single grain, it is conceivable that hibonite relics, which are not visible in polished mounts (refer to Fig. 3b), may be present. The structural formula of gorerite can be simplified in two ways to derive the end-member: 1) $^{R}[Ca(Fe_{2.374}Ti_{0.33}Al_{0.296})]$ $^{S}(Fe_{6.457}Al_{2.543})O_{19}$ $\rightarrow$ $^{R}(CaFe_3)^{S}F_9O19 \rightarrow CaFe_{12}O_{19}$; and 2) $^{R}[Ca(Fe_{2.374}Ti_{0.33}Al_{0.296})]^{S}[^{M1}(Al_{0.597}Fe_{0.403})(Fe_{6.054}Al_{1.946})]O_{19}$ $\rightarrow$ $^{R}(CaFe_3)^{S}(AlFe_8)O_{19} \rightarrow CaAlFe_{11}O_{19}$. The second variant, which considers Al > Fe at the *M*1 site, has been accepted by us for defining the gorerite end-member. We believe that resolving the issue of the end-member formula for gorerite should be addressed through the elaboration of criteria for defining end-member formulas within the magnetoplumbite group. In the recently approved nomenclature of the magnetoplumbite group minerals, such criteria were not presented (Holtstam and Hålenius, 2020).

https://doi.org/10.1180/mgm.2024.30 Published online by Cambridge University Press

BVS calculation for gorerite with different variants of Ti incorporation at the *M*2 and *M*4 (R-block) sites indicate that Ti can simultaneously occupy these two sites, similar to barioferrite (Table 6; Krzątała *et al*., 2018). However, given the low content of TiO_2 (< 3 wt. %) in gorerite (Table 1), accurately determining its position in the gorerite structure remains secondary concern. Meanwhile, the BVS calculation reveals a significant under-bonding of the 12-coordinated ***A***(Ca1) site and four-coordinated *M*3-site (Table 6), which requires further explanation. A similar under-bonding phenomenon at the *A*-site was observed during the investigation of the hibonite structure (Nagashima *et al*., 2010; Krüger *et al*., 2021). The *A*(Ca1) site replaces oxygen within the close-packed layer formed by O3 in the R-block at the (001) plane. Within this layer, Ca is coordinated by six oxygens (6 x Ca-O3 = 2.930(3) Å), while at the upper and lower parts of the layer, it is coordinated to six O5-oxygens (Ca-O5 = 2.781(3) Å). In hibonite-like structures, the *A*-O distances are largely independent of the cation types at the *A*-site (Bermanec *et al*., 1996; Krüger *et al*., 2021). This characteristic results in a high inflexibility of the R-blocks leading to increased distances and under-bonding of the Ca-O bonds in gorerite.

In the case of Fe-bearing hibonite from the 'olive unit' in Israel and gem-quality hibonite from Myanmar, the under-bonding of *M*3 site is attributed to the substantial Mg content present at this site (Nagashima *et al*., 2010; Krüger *et al*., 2021).

Genetic aspects

When describing 'olive' unit rocks, we employ the terms hornfels and paralava, which are essentially identical in mineral composition and originate from the same sedimentary protolith during pyrometamorphic processes. Hornfels, typically finer-grained compared to paralava, undergo transformation in the solid state through a metamorphic mechanism involving recrystallization, with intergranular liquid playing an active role. Paralava formation within the

https://doi.org/10.1180/mgm.2024.30 Published online by Cambridge University Press

'olive' unit occurs during intense melting of the protolith. Notably, hornfelses and paralavas of the 'olive' unit were not homogenized during their formation. This lack of homogenization is evident on a macroscopic scale, with the appearance of rounded hematite segregations (concretions) irregularly dispersed within the rock (Figs. 1b, 2). On a microscopic scale it is characterized by the uneven distribution of ferrite aggregates within the fine-grained silicate matrix (Figs. 3a, 4a, S1a).

Drawing an analogy to the processes of iron ore sintering (as described, for instance, by Webster *et al*., 2017), we can reconstruct a crystallization sequence of minerals in ferrite segregations. During the progressive stage of 'olive' unit paralava formation, hibonite was likely the first mineral to crystallize within the drops of an iron-rich melt at temperatures exceeding 1300°C, possibly during the peak of pyrometamorphism. Concurrently, these metal drops would have reacted with surrounding silicate melt. Subsequently, magnesioferrite and later dorrite would have crystallized. It is probable that magnetite also formed during the peak of pyrometamorphism, and as the temperature decreased, it transformed into maghemite, which was in equilibrium with hematite (Fig. 4c). The decrease in temperature also prompted the reaction of the early-formed hibonite with iron oxides, resulting in its replacement and epitaxial overgrowth by gorerite (Figs. 4b,c; 5c,d).

Within the ferrite drop, a small volume of silicate melt (glass) with elevated Al and Si contents could have formed, which was later replaced by low-temperature minerals such as calcite, tacharanite, or zeolites (Figs. 4b; 5). In ferrite drops with higher barium-content, gorerite is substituted by barioferrite (Fig. 5b). The process of ferrite aggregate formation was finalized by the growth of andradite zones (Figs. 3b; 4c). Therefore, gorerite did not form directly from the melt. Instead, gorerite emerged as a result of a reaction of hibonite (which crystallized earlier)

https://doi.org/10.1180/mgm.2024.30 Published online by Cambridge University Press

with an iron-enriched melt, leading to partial or complete replacement of hibonite by gorerite (Figs. 4b,c; 5c,d).

Interestingly, the phase with an ideal composition, $CaFe_{12}O_{19}$, does not form (it is not stable) in the experimental system $CaO\text{-}Fe_2O_3$. Instead in the stoichiometric melt hematite, harmunite and $CaFe_4O_7$ tend to form (Phillips *et al*., 1956). It's worth noting that nano-sized $CaFe_{12}O_{19}$ has been synthesized using the sol-gel combustion method with its c-parameter significantly smaller than that of gorerite: a = 5.807-6.049 Å, c = 21.325-22.27 Å (Mamatha *et al*., 2017; Deshpande *et al*., 2017; Manjunatha and Rajashekara, 2020; Shinde *et al*., 2020). Impurities added to the experimental system stabilized the structure of $CaFe_{12}O_{19}$. In our case, gorerite crystallization was possible not only due to impurities such as Al, Ti, Cr, Mg, Mn stabilizing its structure (Table 1), but also due to the mechanism of formation – metasomatic replacement and epitaxial overgrowth of early hibonite in the presence of an oxidized melt enriched in iron.

Author Contributions: E.G., B.K. and I.G. contributed to the writing of the draft manuscript, Ye.V., I.O. and E.G. participated in the fieldwork, which led to the discovery of gorerite. E.G., I.G., Ye.V. and K.N. conducted petrological investigations, measured the composition of gorerite and associated minerals, performed Raman and optical studies, and selected grains for structural investigations. B.K. and H.K. performed SC XRD investigation using synchrotron radiation, B.K. refined the gorerite structure. All authors have read and agreed to the published version of the manuscript.

https://doi.org/10.1180/mgm.2024.30 Published online by Cambridge University Press

Acknowledgments: BK and HK acknowledge technical help from Takashi Tomizaki at the synchrotron and V. Olieric for access to the beamline. The authors thank Igor Pekov, Peter Leverett, and an anonymous reviewer for their remarks and comments that improved an earlier version of the manuscript. Investigations were partially supported by the National Science Centre of Poland Grant No. 2021/41/B/ST10/00130 (EG and IG).

Supplementary material. The supplementary material for this article can be found at ….

Competing interests. The authors declare none.

References

Bentor Y.K. (editor) (1960) Israel. In: *Lexique Stratigraphique International, Asie,* Vol. III, (10.2). Centre national de la recherche scientifique, Paris.

Bermanec V., Holtstam D., Sturman D., Criddle A., Back M. and Scavnicar S. (1996) Nežilovite, a new member of the magnetoplumbite group, and the crystal chemistry of magnetoplumbite and hibonite. *Canadian Mineralogist*, **34**, 1287–1297.

Deshpande A.D., Rewatkar K.G. and Nanoti V.M. (2017) Study of morphology and magnetic properties of nanosized particles of zirconium – cobalt substituted calcium hexaferrites. *Materials Today: Proceedings*, **4**, 12174–12179.

Galuskin E.V., Galuskina I.O., Widmer R. and Armbruster, T. (2018) First natural hexaferrite with mixed β’’’-ferrite (b-alumina) and magnetoplumbite structure from Jabel Harmun, Palestinian Autonomy. *European Journal of Mineralogy*, **30**, 559–567.

Galuskin E.V., Krüger B., Galuskina I.O., Krüger H., Vapnik Ye., Pauluhn A. and Olieric V. (2019) Levantite, $KCa_3(Al_2Si_3)O_{11}(PO_4)$, a new latiumite-group mineral from the

https://doi.org/10.1180/mgm.2024.30 Published online by Cambridge University Press

pyrometamorphic rocks of the Hatrurim Basin, Negev Desert, Israel. *Mineralogical Magazine*, **83**, 713–21.

Galuskina I.O., Galuskin E.V., Pakhomova A.S., Widmer, R., Armbruster T., Krüger B., Grew E. S., Vapnik Y., Dzierżanowski P. and Murashko M. (2017) Khesinite, $Ca_4Mg_2Fe^{3+}_{10}O_4[(Fe^{3+}_{10}Si_2)O_{36}]$, a new rhönite-group (sapphirine supergroup) mineral from the Negev Desert, Israel – natural analogue of the SFCA phase. *European Journal of Mineralogy*, **29**, 101–116.

Galuskin E.V., Krüger H., Galuskina I.O., Krüger B., Nejbert K. and Vapnik Y. (2021) Shagamite, IMA 2020-091. CNMNC Newsletter 60. *Mineralogical Magazine*, **85**. https://doi.org/10.1180/mgm.2021.30.

Galuskina I.O., Vapnik Ye., Lazic B., Armbruster T., Murashko M. and Galuskin E.V. (2014) Harmunite $CaFe_2O_4$ – a new mineral from the Jabel Harmun, West Bank, Palestinian Autonomy, Israel. *American Mineralogist*, **99**, 965-975.

Gross S. (1977) The mineralogy of the Hatrurim Formation, Israel. *Geological Survey of Israel Bulletin*, **70**, 1–80.

Holtstam D. and Hålenius U. (2020) Nomenclature of the magnetoplumbite group. *Mineralogical Magazine*, **84**, 376–380.

Iyi N. and Göbbels M. (1996) Crystal structure of the new magnetoplumbite-related compound in the system SrO-Al_2O_3- MgO. *Journal* of *Solid State Chemistry,* **122**, 46–52.

Krause W. and Nolze G. (1996) *POWDER CELL* - a program for the representation and manipulation of crystal structures and calculation of the resulting X-ray powder patterns. *Journal of Applied Crystallography*, **29**, 301-303.

Kreisel, J., Lucazeau G. and Vincent H. (1998) Raman spectra and vibrational analysis of $BaFe_{12}O_{19}$ hexagonal ferrite. *Journal* of *Solid State Chemistry*, **137**, 127–137.

https://doi.org/10.1180/mgm.2024.30 Published online by Cambridge University Press

Krzątała A., Panikorovskii T.L., Galuskina I. and Galuskin E. (2018) Dynamic disorder of Fe^{3+} ions in the crystal structure of natural barioferrite. *Minerals*, **8**, 340.

Kruszewski Ł., Palchik V., Vapnik Y., Nowak K., Banasik K. and Galuskina I. (2021) Mineralogical, geochemical, and rock mechanic characteristics of zeolite-bearing rocks of the Hatrurim Basin, Israel. *Minerals*, *11*, 1062.

Krüger B., Galuskin E.V., Galuskina I.O., Krüger H. and Vapnik Ye. (2021) Kahlenbergite $KAl_{11}O_{17}$, a new *β*-alumina mineral and Fe-rich hibonite from the Hatrurim Basin, the Negev desert, Israel. *European Journal of Mineralogy*, **33**, 341–355.

Nagashaima M., Armbruster T. and Hainschwang T. (2010) A temperature-dependent structure study of gem-quality hibonite from Myanmar. *Mineralogical Magazine*, **74**, 871-885.

Mamathaa Ch., Krishnaiahb M. and Sreedharc B. (2017) Enhancement of magnetic properties of calcium hexaferrites with aluminium substitution. *Procedia Engineering*, **215**, 130–135.

Manjunata B.C. and Rajashekara K.M. (2020) Synthesis and characterization of nano-hexagonal calcium ferrites. *Journal of Nanoscience and Technology*, **6**, 894-896.

Murashko M.N., Chukanov N.V., Mukhanova A.A., Vapnik Ye., Britvin S.N., Polekhovsky Y.S. and Ivakin Y.D. (2011) Barioferrite $BaFe_{12}O_{19}$: A new mineral species of the magnetoplumbite group from the Haturim Formation in Israel. *Geology* of *Ore Deposits,* **53**, 558–563.

Novikov I., Vapnik Ye. and Safonova I. (2013) Mud volcano origin of the Mottled Zone, South Levant. *Geoscience Frontiers*, **4**, 597–619.

Phillips B. and Muan A. (1958) Phase Equilibria in the System CaO-Iron Oxide-SiO_2, in Air. *Journal* of the *American Ceramic Society*, **42**, 413-423.

https://doi.org/10.1180/mgm.2024.30 Published online by Cambridge University Press

Pullar R.C. (2012) Hexagonal ferrites: A review of the synthesis, properties and applications of hexaferrite ceramics. *Progress* in *Materials Science,* **57**, 1191–1334.

Petříček, V., Dušek, M. and Palatinus, L. (2014) Crystallographic Computing System JANA2006: General features. *Zeitschrift für Kristallographie – Crystalline Materials,* 229, 345–352.

Rigaku (2022) CrysAlisProSoftware System, Version 171.42.29, Rigaku Oxford Diffraction Ltd, Yarnton, Oxfordshire, England.

Sharygin, V.V. (2019) A hibonite-spinel-corundum-hematite assemblage in plagioclase-clinopyroxene pyrometamorphic rocks, Hatrurim Basin, Israel: mineral chemistry, genesis and formation temperatures. *Mineralogical Magazine,* **83**, 123–135.

Sharygin V.V., Murashko M.N. (2021) High-chromian gorerite and barioferrite in melilite hornfels at Hatrurim basin, Israel. "Minerals: structure, properties, research methods: materials of the XII All-Russian Youth Scientific Conference (Ekaterinburg, August 26-28, 2021)". Ekaterinburg: Institute of Geology and Geochemistry of the Ural Branch of the Russian Academy of Sciences, 166-168.

Shinde V.S., Dahotre S.G. and Singh L.N. (2020) Synthesis and characterization of aluminium substituted calcium hexaferrite. *Heliyon*, **6**, e03186.

Vapnik Y., Sharygin V.V., Sokol E.V. and Shagam R. (2007) Paralavas in a combustion metamorphic complex: Hatrurim Basin, Israel. *Reviews in Engineering Geology*, 18, 1-21.

Webster N.A.S., Pownceby M.I. and Pattel R. (2017) Fundamentals of silico-ferrite of calcium and aluminium (SFCA) and SFCA-I iron ore sinter bonding phase formation: effects of mill scale addition. *Powder Diffraction*, **32**, 85-89.

Wojdyla J.A., Kaminski J.W., Panepucci E., Ebner S., Wang X., Gabadinho J. and Wang M. (2018) DA+ data acquisition and analysis software at the Swiss Light Source

https://doi.org/10.1180/mgm.2024.30 Published online by Cambridge University Press

macromolecular crystallography beamlines. *Journal of* Synchrotron Radiation, **25**, 293–303.

https://doi.org/10.1180/mgm.2024.30 Published online by Cambridge University Press

Table 1. Chemical composition of gorerite from holotype specimen.

	1			2			3		
	Fig. 3a			Fig. 4a,b			Fig. 5c,d		
wt.%	*n*=5	s.d.	range	*n*=34	s.d.	range	*n*=32	s.d.	range
TiO_2	2.89	0.13	2.72-3.03	1.86	0.24	1.11-2.36	1.73	0.35	1.37-2.08
SiO_2	n.d.			0.07	0.08	0-0.44	0.05	0.05	0-0.10
Fe_2O_3	78.80	0.65	78.12-79.61	75.80	2.13	72.90-79.84	76.50	3.53	71.25-79.66
Mn_2O_3	0.40	0.04	0.32-0.41	0.13	0.08	0-0.27	0.15	0.10	0-0.25
Cr_2O_3	2.45	0.22	2.14-2.64	0.53	0.07	0.40-0.65	0.43	0.18	0.24-0.76
Al_2O_3	7.71	0.51	7.03-8.26	13.48	1.58	10.07-16.13	13.57	3.49	10.52-17.82
BaO	n.d.			n.d.	0.04	0-0.17	0.12	0.41	0-0.95
SrO	n.d.			n.d.	0.06	0-0.23	0.12	0.22	0-0.49
CaO	6.01	0.04	5.96-6.07	6.21	0.19	5.88-6.62	6.07	0.40	5.54-6.40
MgO	1.19	0.02	1.16-1.21	0.87	0.14	0.57-1.06	0.78	0.26	0.60-1.01
Na_2O	0.03	0.03	0-0.07	n.d.	0.02	0-0.08	n.d.		
Total	99.48			98.95			99.52		
				Calculated on 19O					
Ca	0.99			1.00			0.99		
Na	0.01								
Ba							0.01		
Sr							0.01		
A	1.00			1.00			1.01		
Fe^{3+}	9.51			8.95			9.00		
Al	1.46			2.49			2.50		
Mg	0.28			0.20			0.18		
Ti^{4+}	0.35			0.22			0.20		
Cr^{3+}	0.31			0.07			0.05		
Ca	0.04			0.04			0.03		
Mn^{3+}	0.05			0.02			0.02		
Si				0.01			0.01		
B	12			12			12		

n.d. – not detected

https://doi.org/10.1180/mgm.2024.30 Published online by Cambridge University Press

Table 2. Parameters for X-ray data collection and crystal-structure refinement for gorerite.

Crystal data	
Refined chemical formula sum	$CaFe_{8.83}Al_{2.839}Ti_{0.33}O_{19}$
Crystal system	hexagonal
Space group	$P6_3/mmc$ (no. 194)
Unit-cell dimensions	$a = b = 5.8532(4)$Å, $c = 22.7730(2)$ Å $\alpha = 90°$, $\beta = 90°$, $\gamma = 120°$ V = 675.67(7) Å, Z = 2
Z	2
Crystal size	0.012×0.010×0.005 mm
Density (calculated)	4.5697 g/cm^3
Absorption coefficient μ	10.064 mm^{-1}
F000	891
Data collection	
Diffractometer	beamline PXIII -X06DA, Swiss Light Source, PILATUS 2M-F detector
Radiation wavelength	0.70848Å
Detector to sample distance	90 mm
min. & max. theta	3.59°, 36.17°
Reflection ranges	$-9 \le h \le 8$; $-8 \le k \le 8$; $-34 \le l \le 29$
T_{min}, T_{max}	0.886, 0.951
Refinement of structure	
Reflections measured	5092
No. of unique reflections	598
No. of observed unique refl. [I>3σ(I)]	470
Refined parameters	46
Rint	0.096
R_1	0.052
wR_2 *	0.060
Goof	1.31
Δρmin [e Å-3]	-0.89
Δρmax [e Å-3]	0.98

* $w=1/(\sigma^2(F)+0.0001F^2)$

https://doi.org/10.1180/mgm.2024.30 Published online by Cambridge University Press

Table 3. Atom coordinates (x,y,z), equivalent isotropic displacement parameters (U_{eq}, Å^2) and occupancies for gorerite

Atom	site	x	y	z	occupancy	U_{eq}
Ca	*Ca*1	0.666667	0.333333	0.25	1	0.0665(12)
Al1/Fe1	*M*1	0	0	0	0.597(13) Al1+0.403(13) Fe1	0.0198(5)
Fe2/Ti2	*M*2	0	0	0.25	0.67(4) Fe2 + 0.33(4) Ti2	0.0277(4)
Fe3/Al3	*M*3	0.333333	0.666667	0.02743(4)	0.774(14) Fe3 + 0.226(14) Al3	0.0198(3)
Fe4/Al4	*M*4	0.333333	0.666667	0.19015(4)	0.852(15) Fe4 + 0.148(15) Al4	0.0203(3)
Fe5/Al5	*M*5	0.16821(4)	0.33641(9)	-0.10898(3)	0.751(13) Fe5 + 0.249(13) Al5	0.0202(2)
O1	O	0	0	0.1523(2)	1	0.0232(11)
O2	O	0.666667	0.333333	0.0563(2)	1	0.0248(11)
O3	O	0.1807(3)	0.3614(6)	0.25	1	0.0323(13)
O4	O	0.8461(2)	0.1539(2)	0.55234(13)	1	0.0243(8)
O5	O	0.50480(19)	1.0096(4)	0.15140(15)	1	0.0264(9)

Table 4. Anisotropic displacement parameters (Å^2) for gorerite

Site	U^{11}	U^{22}	U^{33}	U^{12}	U^{13}	U^{23}
*Ca*1	0.0729(15)	0.0729(15)	0.0536(18)	0.0365(7)	0	0
*M*1	0.0190(6)	0.0190(6)	0.0214(9)	0.0095(3)	0	0
*M*2	0.0194(4)	0.0194(4)	0.0443(9)	0.0097(2)	0	0
*M*3	0.0183(4)	0.0183(4)	0.0229(5)	0.00917(18)	0	0
*M*4	0.0193(3)	0.0193(3)	0.0222(5)	0.00967(17)	0	0
*M*5	0.0188(3)	0.0180(3)	0.0237(4)	0.00899(16)	0.00003(8)	0.00007(15)
O1	0.0210(12)	0.0210(12)	0.028(2)	0.0105(6)	0	0
O2	0.0223(11)	0.0223(11)	0.030(2)	0.0111(6)	0	0
O3	0.0426(19)	0.0239(16)	0.0241(19)	0.0120(8)	0	0
O4	0.0226(9)	0.0226(9)	0.0278(13)	0.0115(9)	0.0002(4)	-0.0002(4)
O5	0.0226(9)	0.0225(12)	0.0339(16)	0.0113(6)	0.0016(4)	0.0031(8)

https://doi.org/10.1180/mgm.2024.30 Published online by Cambridge University Press

Table 5. Selected bond distances (Å) for gorerite

atom-	atom	distance (Å)	
Ca1	O3	2.930(3)	×6
	O5	2.781(3)	×6
	mean	2.856	
Al1/Fe1	O4	1.963(2)	×6
Fe2/Ti2	O3	1.832(3)	×3
	O1	2.225(5)	×2
	mean	1.989	
Fe3/Al3	O2	1.908(5)	
	O4	1.906(2)	×3
	mean	1.907	
Fe4/Al4	O3	2.062(2)	×3
	O5	1.949(2)	×3
	mean	2.006	
Fe5/Al5	O1	1.970(3)	
	O2	2.059(3)	
	O4	2.084(2)	×2
	O5	1.919(3)	×2
	mean	2.006	

https://doi.org/10.1180/mgm.2024.30 Published online by Cambridge University Press

Table 6. Weighted bond valences (in valence units) for gorerite

		O1	O2	O3	O4	O5	Sum
site	R-block						
A/Ca1	Ca			$0.07^{6\rightarrow 2\downarrow}$		$0.11^{6\rightarrow\downarrow}$	1.08
*M*2	0.67Fe+0.33Ti	$0.30^{2\rightarrow\downarrow}$		$0.87^{3\rightarrow\downarrow}$			3.21
	0.898Fe+0.102Al	$0.275^{2\rightarrow\downarrow}$		$0.795^{3\rightarrow\downarrow}$			*2.94*
*M*4	0.852Fe+0.148Al			$0.42^{3\rightarrow 2\downarrow}$		$0.57^{3\rightarrow\downarrow}$	2.97
	0.519Fe+0.481Ti			$0.48^{3\rightarrow 2\downarrow}$		$0.645^{3\rightarrow\downarrow}$	*3.375*
	0.61Fe+0.35Ti+0.04Al			$0.46^{3\rightarrow 2\downarrow}$		$0.625^{3\rightarrow\downarrow}$	*3.255*
	S-block						
*M*1	0.597Al+0.403Fe				$0.47^{6\rightarrow\downarrow}$		2.82
*M*3	0.774Fe+0.226Al		$0.62^{\rightarrow\downarrow}$		$0.62^{3\rightarrow\downarrow}$		2.48
*M*5	0.751Fe+0.249Al	$0.52^{\rightarrow 3\downarrow}$	$0.41^{\rightarrow 3\downarrow}$		$0.38^{2\rightarrow 2\downarrow}$	$0.60^{2\rightarrow 2\downarrow}$	2.89
	Sum (only first options for *M*2 and *M*4)	1.86	1.85	1.85	1.85	1.88	

https://doi.org/10.1180/mgm.2024.30 Published online by Cambridge University Press